Research in Astronomy and Astrophysics, 24:125009 (12pp), 2024 December https://doi.org/10.1088/1674-4527/ad8eae

ALMA and GMRT Studies of Dust Continuum Emission and Spectral Lines Toward Oort Cloud Comet C/2022 E3 (ZTF)

Arijit Manna[1], Sabyasachi Pal[1], Sekhar Sinha[2], and Sushanta Kumar Mondal[2]
[1] Department of Physics and Astronomy, Midnapore City College, Paschim Medinipur 721129, India; amanna.astro@gmail.com
[2] Department of Physics, Sidho-Kanho-Birsha University, Ranchi Road, Purulia 723104, India
Received 2024 September 21; revised 2024 October 29; accepted 2024 October 31; published 2024 December 2

Abstract

The atomic and molecular compounds of cometary ices serve as valuable knowledge into the chemical and physical properties of the outer solar nebula, where comets are formed. From the cometary atmospheres, the atoms and gas-phase molecules arise mainly in three ways: (i) the outgassing from the nucleus, (ii) the photochemical process, and (iii) the sublimation of icy grains from the nucleus. In this paper, we present the radio and millimeter wavelength observation results of Oort cloud non-periodic comet C/2022 E3 (ZTF) using the Giant Metrewave Radio Telescope (GMRT) band L and the Atacama Large Millimeter/submillimeter Array (ALMA) band 6. We do not detect continuum emissions and an emission line of atomic hydrogen (H I) at rest frequency 1420 MHz from this comet using the GMRT. Based on ALMA observations, we detect the dust continuum emission and rotational emission lines of methanol (CH_3OH) from comet C/2022 E3 (ZTF). From the dust continuum emission, the dust production ($Af\rho$) activity of comet ZTF is 2280 ± 50 cm. Based on LTE spectral modeling, the column density and excitation temperature of CH_3OH toward C/2022 E3 (ZTF) are $(4.50 \pm 0.25) \times 10^{14}$ cm^{-2} and 70 ± 3 K respectively. The integrated emission maps show that CH_3OH was emitted from the coma region of the comet. The production rate of CH_3OH toward C/2022 E3 (ZTF) is $(7.32 \pm 0.64) \times 10^{26}$ molecules s^{-1}. The fractional abundance of CH_3OH with respect to H_2O in the coma of the comet is 1.52%. We also compare our derived abundance of CH_3OH with the existence modeled value, and we see the observed and modeled values are quite similar. We claim that CH_3OH is formed via the subsequential hydrogenation of formaldehyde (H_2CO) on the grain surface of comet C/2022 E3 (ZTF).

Key words: comets: general – planets and satellites: composition – radio continuum: planetary systems – submillimeter: planetary systems – astrochemistry

1. Introduction

Comets are kilometer-sized, ice-rich objects made of refractory, and volatile chemical compounds (Ehrenfreund & Charnley 2000). This is the most pure remnant of the formation of the solar system, just 4.6 billion years ago. Comets provide the most excellent insight to study the volatile compositions of the solar protoplanetary disks since they gather some of the solar system's most ancient and primordial substances, including ice. Previous studies show that water (H_2O) and different organic matter may have reached the early Earth through comets as well (Hartogh et al. 2011). Since comets travel in the interstellar medium (ISM), they collect complex compounds, including amino acids (R–CH(NH_2)–COOH), from molecular clouds, star formation regions, and protoplanetary disks and transport them into the planetary atmosphere via collision with the planet (Ehrenfreund & Charnley 2000). Thus, it is crucial to understand the variability in composition and isotopic ratios of cometary material to evaluate such scenarios (Altwegg & Bockelée-Morvan 2003; Bockelée-Morvan et al. 2015). Previously, more than 60 molecular compounds were identified toward comet 67P/Churyumov-Gerasimenko between 2014 and 2016 using the Rosetta Orbiter Spectrometer for Ion and Neutral Analysis (ROSINA), and their chemical compositions have been investigated using both in situ and remote ways (see Biver & Bockelée-Morvan 2019 and references therein). In recent years, high-sensitivity ground-based millimeter-wavelength telescopes have identified over 25 complex molecular compounds from cometary atmospheres (see Figure 1 of Biver & Bockelée-Morvan 2019 and references therein). Earlier, Altwegg et al. (2016) detected the simplest amino acid glycine (NH_2CH_2COOH), phosphorus (P), and different complex compounds from the 67P/Churyumov-Gerasimenko using ROSINA. After that, Hadraoui et al. (2019) made a chemical model and showed that NH_2CH_2COOH is ejected from the nucleus due to the sublimation of ice from the dust particles. Recently, centimeter and millimeter-wavelength observations found evidence of atomic hydrogen (H I) and molecular emission lines of HCN, HNC, CH_3OH, CS, CH_3CN, H_2CO, SO,

HC_3N, and H_2S from comet C/2020 F3 (NEOWISE) (Biver et al. 2022; Pal & Manna 2024).

One of the most common interstellar molecules, methanol (CH_3OH), was discovered in space for the first time over 54 yr ago (Ball et al. 1970). In the ISM, CH_3OH has been found in gaseous and solid forms (Ehrenfreund & Charnley 2000). The evidence of CH_3OH is found in hot molecular cores, hot corinos, dark clouds, the Galactic Center, and protoplanetary disks (Herbst & van Dishoeck 2009; Thiel et al. 2017; Manigand et al. 2020; Booth et al. 2021; Chen et al. 2022). Earlier, Drabek-Maunder et al. (2019) claimed the detection of CH_3OH with transition $J = 5$ (1,1)–4(1,1) toward Saturn's moon Enceladus using the IRAM 30 m telescope, but a single transition line of complex molecules does not provide a secure detection. So, it is challenging to believe the detection of CH_3OH toward Enceladus by Drabek-Maunder et al. (2019). The emission lines of CH_3OH are also found in the cometary atmosphere. In the solar system, the CH_3OH lines were first found from comets Austin (1990 V) and Levy (1990 XX) with the IRAM 30 m telescope (Bockelée-Morvan et al. 1994a). The emission lines of CH_3OH were also found from comets P/Swift-Tuttle (1992) (Bockelée-Morvan et al. 1994b), Hyakutake (C/1996 B2) (Womack et al. 1997), Lee (C/1999 H1) (Biver et al. 2000), Hale-Bopp (C/1995 O1) (Biver et al. 1999a), P/Halley (Eberhardt et al. 1994), C/2012 S1 (ISON) (Agúndez et al. 2014), C/2013 R1 (Lovejoy) (Agúndez et al. 2014), C/2012 F6 (Lemmon) (Bøgelund & Hogerheijde 2017), C/2012 K1 (PanSTARRS) (Cordiner et al. 2017), 46P/Wirtanen (Cordiner et al. 2023), and C/2020 F3 (NEOWISE) (Biver et al. 2022). Previously, Greenberg (1982) demonstrated that the chemical composition of cometary grains exhibits a strong similarity to those found in the ISM and circumstellar disks, which indicates the formation pathways of CH_3OH toward the cometary atmosphere are quite similar to those of interstellar grains. Earlier, Garrod (2019) showed that the formation pathways of CH_3OH toward a cometary atmosphere are similar to those in star formation regions.

C/2022 E3 (ZTF) (hereafter ZTF) is a long-period Oort-cloud comet (initial semimajor axis of 2000 au) that was discovered on 2022 March 2, using the Zwicky Transient Facility at a heliocentric distance of 4.3 au (Bolin et al. 2022). The orbital properties of comet ZTF are shown in Table 1. This comet came closest to Earth on 2023 February 1, at a distance of 0.28 au. The close distance indicates that comet ZTF is a near-Earth object. In 2022 March, comet ZTF showed interesting cometary features, including a green coma of diatomic carbon (C_2), a yellow dust tail, and a thin ion tail. After the identification of this comet, Liu & Liu (2024) observed that the heliocentric distance of ZTF decreased with time, which signifies the sublimation of volatile species from the grain surface of the nucleus due to the acceleration of solar heat, thus enhancing the luminosity of the green coma. The production rates of OH and H_2O toward comet ZTF were $Q_{OH} = 3.51 \times 10^{28}\ s^{-1}$ and $Q_{H_2O} = 4.8 \times 10^{28}\ s^{-1}$, respectively (Jehin et al. 2022; Schleicher et al. 2023). The production rates of CN, C_3, and C_2 on 2023 March 10 were $(5.43 \pm 0.11) \times 10^{25}\ s^{-1}$, $(2.01 \pm 0.04) \times 10^{24}\ s^{-1}$, and $(3.08 \pm 0.50) \times 10^{25}\ s^{-1}$, respectively (Bolin et al. 2024). Liu & Liu (2024) reported that the size of the nucleus of the comet ZTF is 2.79 km. In 2023 February, the Trivandrum Observatory post-perihelion observation data showed that the apparent sizes of the tail and head of the comet ZTF were noticeably decreased (Jayakrishnan et al. 2023). Recently, Biver et al. (2024) detected several rotational emission lines of different organic molecules, including CH_3OH, toward comets ZTF and C/2021 A1 (Leonard) using the IRAM 30 m telescope. Biver et al. (2024) also claimed the detection of ethylene glycol ($(CH_2OH)_2$) and methyl cyanide (CH_3CN) from comets ZTF and C/2021 A1 (Leonard). Biver et al. (2024) also did not discuss the formation pathways of CH_3OH toward comets ZTF and C/2021 A1 (Leonard).

Table 1
Orbital Properties of Comet ZTF

Parameter	Symbol	Value
Orbit eccentricity	e	1.0000290
Orbit inclination	i	109.°16920
Perihelion distance	q	1.1126880 au
Aphelion distance	Q	2800 au
Semimajor axis	a	−4087 au
Orbital period	P	50,000 yr
Time of perihelion passage	T	2459957.18000 JD
Longitude of ascending node	Ω	302.°53990
Argument of perihelion	ω	145.°80970
Longitude of perihelion	L	315.°11506
Latitude of perihelion	B	32.°05853
Classification	...	Nearly isotropic ($a > 10{,}000$ au)

Note. The orbital parameters of comet ZTF are taken from Bolin et al. (2022) and the NASA JPL Horizons System.

This paper presents the centimeter and millimeter-wavelength observations of comet ZTF using the high-resolution Giant Metrewave Radio Telescope (GMRT) and Atacama Large Millimeter/submillimeter Array (ALMA). We also detected the rotational emission lines of CH_3OH from the coma region of this comet. The observational methods and data analysis techniques used in this study are described in Section 2. The results and discussions of the detection of dust continuum and line emissions are shown in Section 3. The conclusions are presented in Section 4.

2. Observations and Data Reductions

2.1. Atacama Large Millimeter/Submillimeter Array (ALMA)

We used the publicly available archival data of comet ZTF, which was observed on 2023 March 2, utilizing the high-

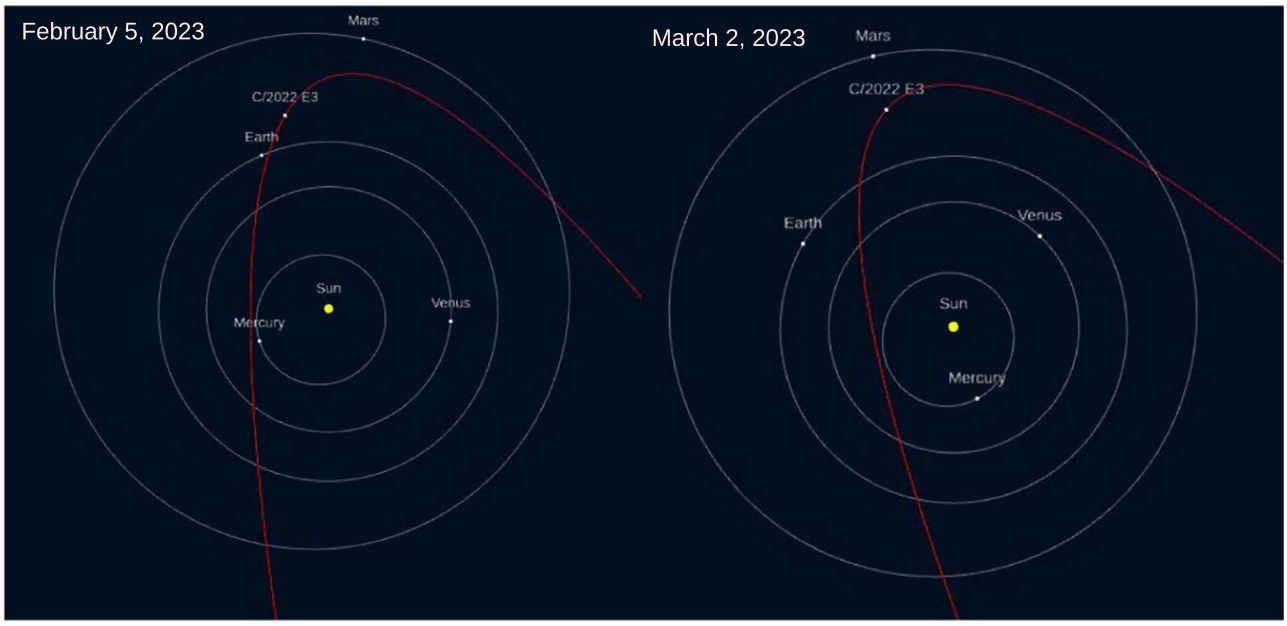

Figure 1. Orbital configuration of comet C/2022 E3 (ZTF) and inner solar system on 2023 February 5 (date of GMRT observation) and 2023 March 2 (date of ALMA observation).

resolution ALMA 12 m arrays with band 6 (PI: Martin Cordiner, ID: 2022.1.00997.T). This observation aimed to study the millimeter-wavelength dust continuum emission and detection of volatile molecules. On 2023 March 2, the distance between the comet ZTF and Earth was 0.96 au. Similarly, the distance between ZTF and the Sun was 1.35 au. The orbital configuration of comet ZTF on 2023 March 2 is illustrated in Figure 1. This observation was carried out in the frequency ranges of 223.85–225.73 GHz, 225.91–227.79 GHz, 239.01–239.25 GHz, 239.89–240.01 GHz, 240.78–240.90 GHz, and 241.67–243.55 GHz with a spectral resolution of 976.56 kHz. A total of 39 antennas were used during the observation. The minimum and maximum baselines were 15.3 and 783.1 m respectively. The on-source integration time was 44.352 m. During the observation, the comet was continuously tracked, and the phase center position in the sky was updated in real-time using the JPL Horizons orbital solution #JPL 81. During the observation of comet ZTF, the flux and bandpass calibrator were taken as J0423–0120. Similarly, J0442–0017 was used as a phase calibrator.

For the analysis of the raw data of ZTF, we used the Common Astronomy Software Applications (CASA 5.4.1) with standard pipeline scripts delivered by the Joint ALMA Observatory (JAO; CASA Team et al. 2022). For flux calibration, we applied the task SETJY with the Perley–Butler 2017 flux calibrator model (Perley & Butler 2017). We also used the pipeline tasks HIFA_BANDPASSFLAG and HIFA_-FLAGDATA to remove the bad antenna data. After analyzing the raw data, we split the target source (ZTF_C2022_E3) with the help of the CASA task MSTRANSFORM. Before imaging, we subtract the continuum from the visibilities by fitting the second-order polynomial to the line-free channels in all spectral windows. We also employed the CASA task CVEL for Doppler correction to the rest frame of the comet. We made the dust continuum and spectral images of ZTF using the task TCLEAN with Hogbom deconvolution and the SPEC = CUBE parameter. To make the dust continuum emission images, we used line-free channels. At last, we corrected the primary beam pattern in both continuum and spectral images using the task IMPBCOR.

2.2. Giant Metrewave Radio Telescope (GMRT)

Comet ZTF was also observed on 2023 February 5, using the GMRT band L (1050–1450 MHz). GMRT is located in Khodad near Pune in India (PI: Arijit Manna, ID: ddtC267). This observation aimed to study the radio wavelength continuum emission in frequency ranges of 1050–1450 MHz and the emission/absorption line of atomic H I at 1420 MHz. On 2023 February 5, the distance between the ZTF and Earth was 0.30 au. The distance between ZTF and the Sun was 1.16 au on that day. The orbital configuration of comet ZTF on 2023 February 5 is depicted in Figure 1. During the observation, a total of 30 fully steerable, 45 m diameter antennas were used, with minimum and maximum baselines of ∼100 m and ∼25 km, respectively. The National Centre for Radio Astrophysics (NCRA), a division of the esteemed Tata Institute of Fundamental Research (TIFR), operates this radio telescope. A total of 8192 channels were used with a spectral

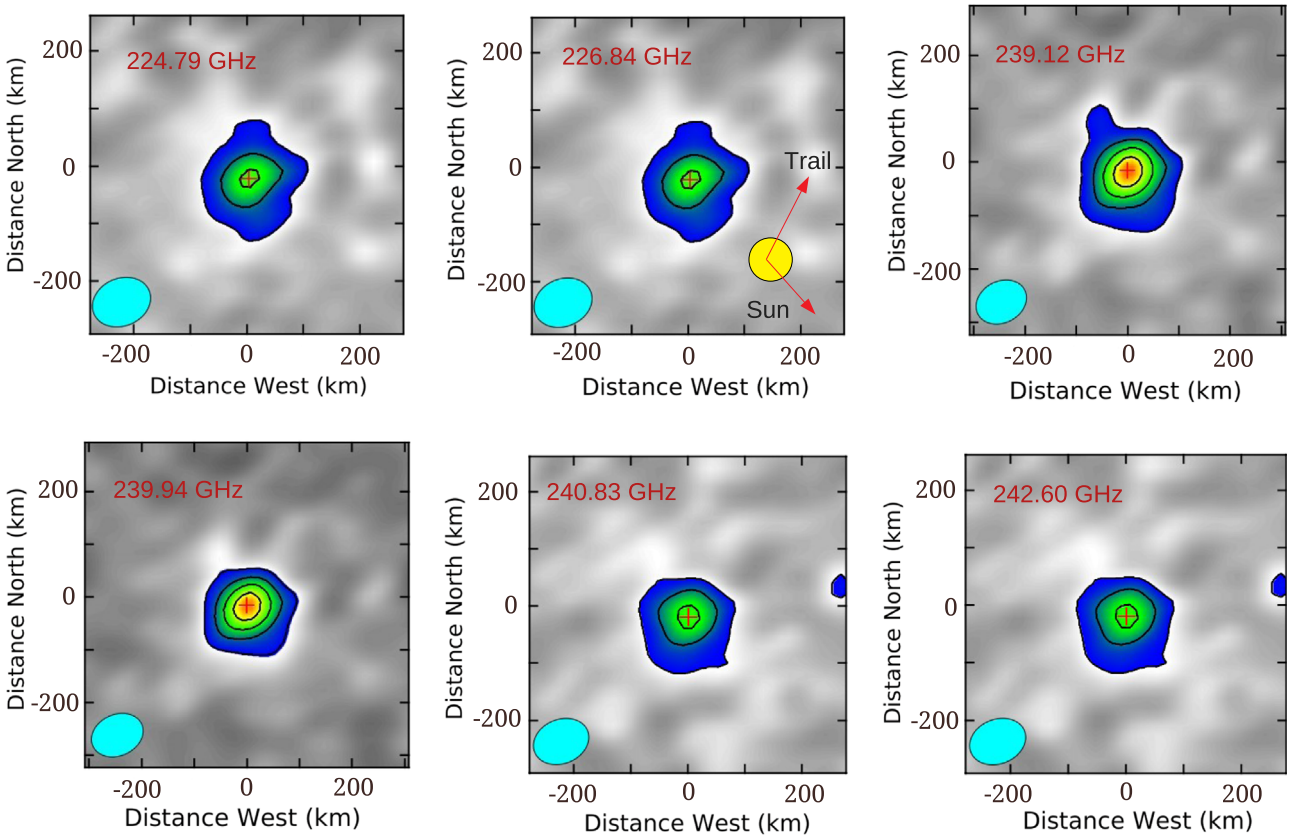

Figure 2. Millimeter-wavelength dust continuum images of comet ZTF. The direction of the Sun and the motion of the comet are shown in the first-panel image. The cyan-colored circles are the synthesized beam of the dust continuum images. The contour levels start at 3σ and increase by a factor of $\sqrt{2}$. The cross sign is the comet position, which is provided by NASA JPL Horizons.

resolution of 0.0488 MHz. The on-source integration time was 3 hr and 15 minutes. During the observation, quasar 3C 147 was used as a flux and phase calibrator.

We followed the standard calibration method using CASA to reduce the data of comet ZTF. We import the raw GMRT data in CASA using the task IMPORTGMRT. During calibration, we remove the bad spectral channels and damaged antenna data. To calibrate the flux, we used the SETJY task, utilizing the Perley–Butler 2017 flux calibrator model (Perley & Butler 2017). We also made the bandpass calibration using 3C 147. After gain calibration and transferring the gain calibration to the target, we applied the task MSTRANSFORM to split the target data. We made the continuum emission images of ZTF with w-projection and the multi-frequency synthesis mode with 2nd-order expansion (Rau & Cornwell 2011). We also used the GAINCAL and APPLYCAL tasks for better image sensitivity. After making the continuum emission images, we subtracted the continuum emission from the visibility using the task UVCONTSUB. We made the spectral images using the TCLEAN task with the SPECMODE = CUBE parameter. We also applied the task WPBGMRT for primary beam correction of the continuum and spectral images.

3. Result and Discussion

3.1. Results Based on ALMA Data

3.1.1. Dust Continuum Emission Toward Comet ZTF

We observed that the comet ZTF was detected in the frequency ranges of 224.79–242.60 GHz, as shown in Figure 2. To estimate the dust continuum parameters of comet ZTF, we fitted the two-dimensional (2D) Gaussian using the CASA task IMFIT over the cometary area with a circle of radius $1\farcs7$. The physical parameters are listed in Table 2. The directions of motion of comet ZTF and the Sun are shown in Figure 2. Comet ZTF is not resolved in the frequency ranges of 224.79–242.60 GHz as the deconvolved source sizes are smaller than the synthesized beam sizes. We plot the spectral energy distribution (SED) of ZTF in the frequency range of 224.79–242.60 GHz. After SED plotting, we fitted the comet flux values using the blackbody model with the help of the

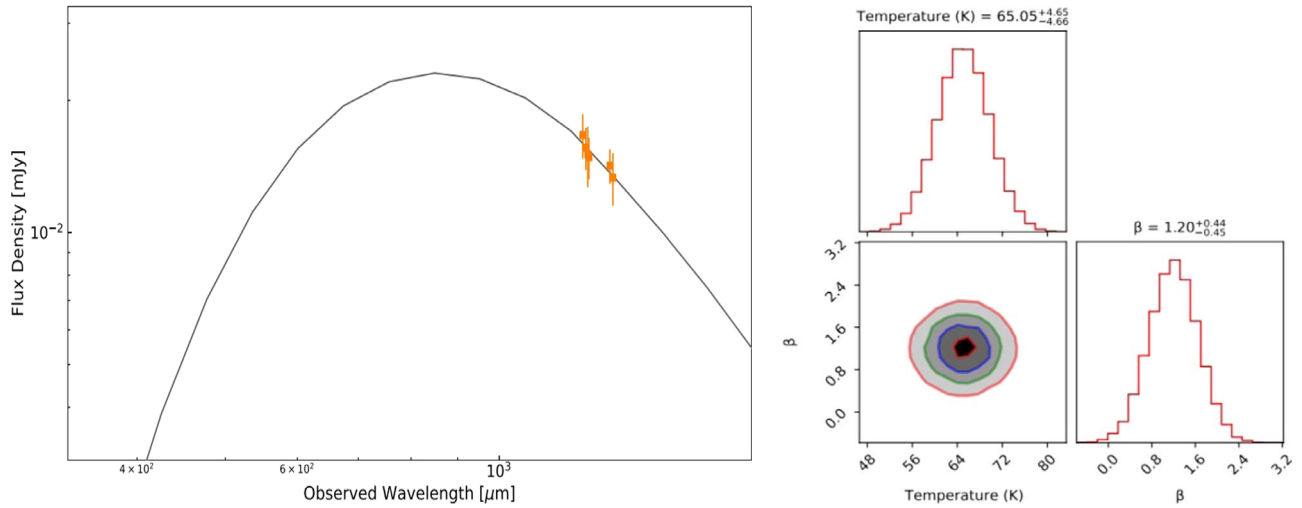

Figure 3. SED plot of comet ZTF based on ALMA band 6 observations (left panel). In the SED plot, the solid orange lines are the fluxes of ZTF with error bars, and the black line indicates the best-fitted SED with the blackbody model. The right panel shows a corner diagram demonstrating the results of our MCMC parameter estimation for the SED model. The diagonal panels display one-dimensional histograms representing the marginalized posterior distributions for dust temperature and dust spectral index (β). Meanwhile, the off-diagonal panels illustrate 2D projections of the posterior probability distributions, showcasing the correlations between each pair of parameters.

Table 2
Dust Continuum Emission Properties of Comet ZTF Based on ALMA Data

Frequency (GHz)	Integrated Flux (μJy)	Peak Flux (μJy beam^{-1})	rms (μJy)	Synthesized Beam ($''$)	Deconvolved Source Size ($''$)
224.79	124 ± 17	120 ± 10	9.45	$0.''53 \times 0.''42$	$0.''51 \times 0.''44$
226.84	132 ± 49	106 ± 12	5.87	$0.''53 \times 0.''41$	$0.''49 \times 0.''42$
239.12	138 ± 17	109 ± 13	7.52	$0.''50 \times 0.''39$	$0.''47 \times 0.''38$
239.94	140 ± 25	112 ± 9	5.20	$0.''50 \times 0.''39$	$0.''48 \times 0.''38$
240.83	145 ± 38	115 ± 10	4.68	$0.''50 \times 0.''39$	$0.''48 \times 0.''37$
242.60	155 ± 32	120 ± 15	6.68	$0.''50 \times 0.''39$	$0.''49 \times 0.''38$

Python package ASTROPY (version 5.0). We used the Markov Chain Monte Carlo (MCMC) algorithm to fit the blackbody model over the observed flux values. The SED plot and corner diagram based on MCMC analysis are shown in Figure 3. After SED analysis, we found the dust temperature and dust spectral index (β) of comet ZTF were 65.05 ± 4.65 K and 1.20 ± 0.44 respectively.

Now, we estimate the activity of dust production (Afρ) of comet ZTF using the following equation (A'Hearn et al. 1984)

$$\mathrm{Af}\rho = \frac{4\, R_h^2\, \Delta^2}{\rho} \frac{F_{\mathrm{com}}}{F_{\odot}}. \quad (1)$$

In Equation (1), R_h is the distance between comet and Sun in astronomical unit, Δ is the distance between Earth and comet in cm, F_{com} is the flux of the comet in the unit of erg cm^{-2} s^{-1}, $\rho \sim 6500$ km is the nucleocentric distance of the comet ZTF (Bolin et al. 2024), and $F_{\odot}$ is the solar flux in the unit of erg cm^{-2} s^{-1} at 1 au. The solar flux is taken from the high-resolution solar spectrum of Kurucz et al. (1984). During the estimation of Afρ, we used the flux value at a frequency of 242.60 GHz. Using Equation (1), the calculated value of Afρ of comet ZTF, based on ALMA data, is 2280 ± 50 cm, which is quite similar to the estimated value of Jehin et al. (2023). Recently, Bolin et al. (2024) estimated the value of Afρ in optical wavelengths toward comet ZTF as 1483 ± 40 cm, which is smaller than the estimated value of Afρ using ALMA data in millimeter wavelengths. Our estimated higher value of Afρ using the ALMA data indicates a high level of dust production due to the close distance between ZTF and the Sun during our observation.

Table 3
Comparison of the Activity of Dust Production (Afρ) with Comet ZTF and other Comets

Comet	Afρ (cm)	R_h (au)	Reference
C/2023 E3 (ZTF)	2280 ± 50	1.35	This study
4P/Faye	1146.0 ± 1.2	1.62	Gillan et al. (2024)
6P/d'Arrest	203.8 ± 1.5	1.54	Gillan et al. (2024)
11P/Tempel-Swift-LINEAR	17.8 ± 0.3	1.39	Gillan et al. (2024)
108P/Ciffreo	146.2 ± 1.5	1.67	Gillan et al. (2024)
114P/Wiseman-Skiff	76.7 ± 0.3	1.59	Gillan et al. (2024)
132P/Helin-Roman-Alu	128.6 ± 0.5	1.70	Gillan et al. (2024)
156P/Russell-LINEAR	681.6 ± 0.4	1.35	Gillan et al. (2024)
254P/McNaught	360.0 ± 6.5	3.68	Gillan et al. (2024)
398P/Boattini	72.1 ± 0.1	1.31	Gillan et al. (2024)
409P/LONEOS-Hill	53.6 ± 1.0	1.75	Gillan et al. (2024)
425P/Kowalski	63.3 ± 3.6	2.90	Gillan et al. (2024)
449P/Leonard (2020 S6)	8.2 ± 0.6	1.88	Gillan et al. (2024)
P/2019 LD2 (ATLAS)	303.4 ± 21.7	4.61	Gillan et al. (2024)
P/2020 T3 (PanSTARRS)	17.5 ± 0.5	1.47	Gillan et al. (2024)
P/2020 U2 (PanSTARRS)	90.8 ± 0.8	1.88	Gillan et al. (2024)
P/2020 WJ5 (Lemmon)	193.4 ± 16.1	5.07	Gillan et al. (2024)
P/2021 Q5 (ATLAS)	41.0 ± 0.9	1.27	Gillan et al. (2024)
67P/Churyumov-Gerasimenko	233 ± 12	1.36	Schleicher (2006)
P/Halley	20,400 ± 110	1.53	Schleicher et al. (1998)
C/2014 UN_{271} (Bernardinelli-Bernstein)	15,000 ± 250	20	Lellouch et al. (2022)

Now, we compare the Afρ value of the comet ZTF with different dynamical types of other comets, as shown in Table 3. After comparison, we observe that comet P/Halley exhibits a higher Afρ at R_h of 1.53 au. Similarly, we found the Afρ value of comet ZTF is 2280 ± 50 cm at R_h of 1.35 au, which is higher than the rest of the comets but lower than the comet P/Halley and C/2014 UN_{271} (Bernardinelli-Bernstein). We found different Afρ values for different comets owing to the different grain sizes, perihelion distances, and ice compositions, which produced more dust as ice vaporized and released dust particles.

3.1.2. Methanol (CH_3OH) Toward Comet ZTF

We extracted the molecular spectra from the spectral images by making a 0.″8 diameter circular region over the cometary area. The synthesized beam sizes of the spectral images in the frequency ranges of 223.85–225.73 GHz, 225.91–227.79 GHz, 239.01–239.25 GHz, 239.89–240.01 GHz, 240.78–240.90 GHz, and 241.67–243.55 GHz were 0.″50 × 0.″39, 0.″51 × 0.″39, 0.″51 × 0.″38, 0.″50 ×0.″38, 0.″50 × 0.″39, and 0.″51 × 0.″39 respectively. For spectral analysis, we used the CASSIS software (Vastel et al. 2015). For the detection of the rotational emission lines of CH_3OH, we used the Local Thermodynamic Equilibrium (LTE) model with the Cologne Database for Molecular Spectroscopy (CDMS) databases (Müller et al. 2005). To fit the LTE spectral model to the observed emission lines of CH_3OH, we utilized the MCMC algorithm within the CASSIS software package. After spectral analysis, we detected a total of 15 transition lines of CH_3OH from the comet ZTF. The detected emission lines of CH_3OH exhibited upper state energies (E_{up}) ranging from 34.82 to 130.82 K. CH_3OH is a slightly asymmetric top molecule with an internal torsional motion of CH_3 around the molecular symmetry axis relative to the OH radical. The transitions of CH_3OH are explained by J, $\pm K_a$, and Γ. In transitions of CH_3OH, we used $\Gamma = A$, where Γ is associated with the "–" or "+" sign that indicates the parity. Similarly, we also used the $\Gamma = E$ in the transitions of CH_3OH because, in the absence of parity, the energy levels (E1 and E2) of CH_3OH are distinguished by $\pm K$. After detection of the rotational emission lines of CH_3OH, we obtained molecular transitions ($J'_{K'_a\Gamma'}$–$J''_{K''_a\Gamma''}$), upper state energy (E_u) in K, Einstein coefficients (A_{ij}) in s^{-1}, line intensity ($S\mu^2$) in Debye^2, full-width at half maximum (FWHM) in km s^{-1}, optical depth (τ), and integrated intensities ($\int T_{mb} dV$) in K km s^{-1}. The detected emission lines and spectral line parameters of CH_3OH are shown in Figure 4 and Table 4. We also observed that the detected emission lines of CH_3OH are optically thin. After spectral line analysis using the LTE model, we found the column density and excitation temperature of CH_3OH are $(4.50 \pm 0.25) \times 10^{14}$ cm^{-2} and 70 ± 3 K respectively. During LTE fitting, we used the source size ∼0.″5. To verify the temperature of CH_3OH, we also made the rotational diagram of CH_3OH, which is shown in Figure 4. The methods and theory of the rotational diagram are well discussed in Manna & Pal (2024). After the rotational diagram, we found the rotational temperature of CH_3OH is 72 ± 12 K, which is very close to the excitation temperature of CH_3OH. Recently, Biver et al. (2024) also claimed the detection of CH_3OH toward comet ZTF, and they estimated the rotational temperature of CH_3OH is 58 ± 4 K using the rotational diagram. The derived rotational temperature of CH_3OH by Biver et al. (2024) is lower than that of the present paper. The estimated rotational temperature of CH_3OH by Biver et al. (2024) is less because it is measured by the IRAM 30 m single dish, whose resolution is much less than the present observation. Biver et al. (2024) could not study the spatial distribution of CH_3OH toward ZTF.

After the detection of the emission lines of CH_3OH, we also made the integrated intensity maps of CH_3OH based on four high-intensity lines using the CASA task IMFIT. The integrated intensity maps of CH_3OH toward comet ZTF are displayed in Figure 5. The integrated intensity maps clearly show that the CH_3OH emits from the inner coma region of

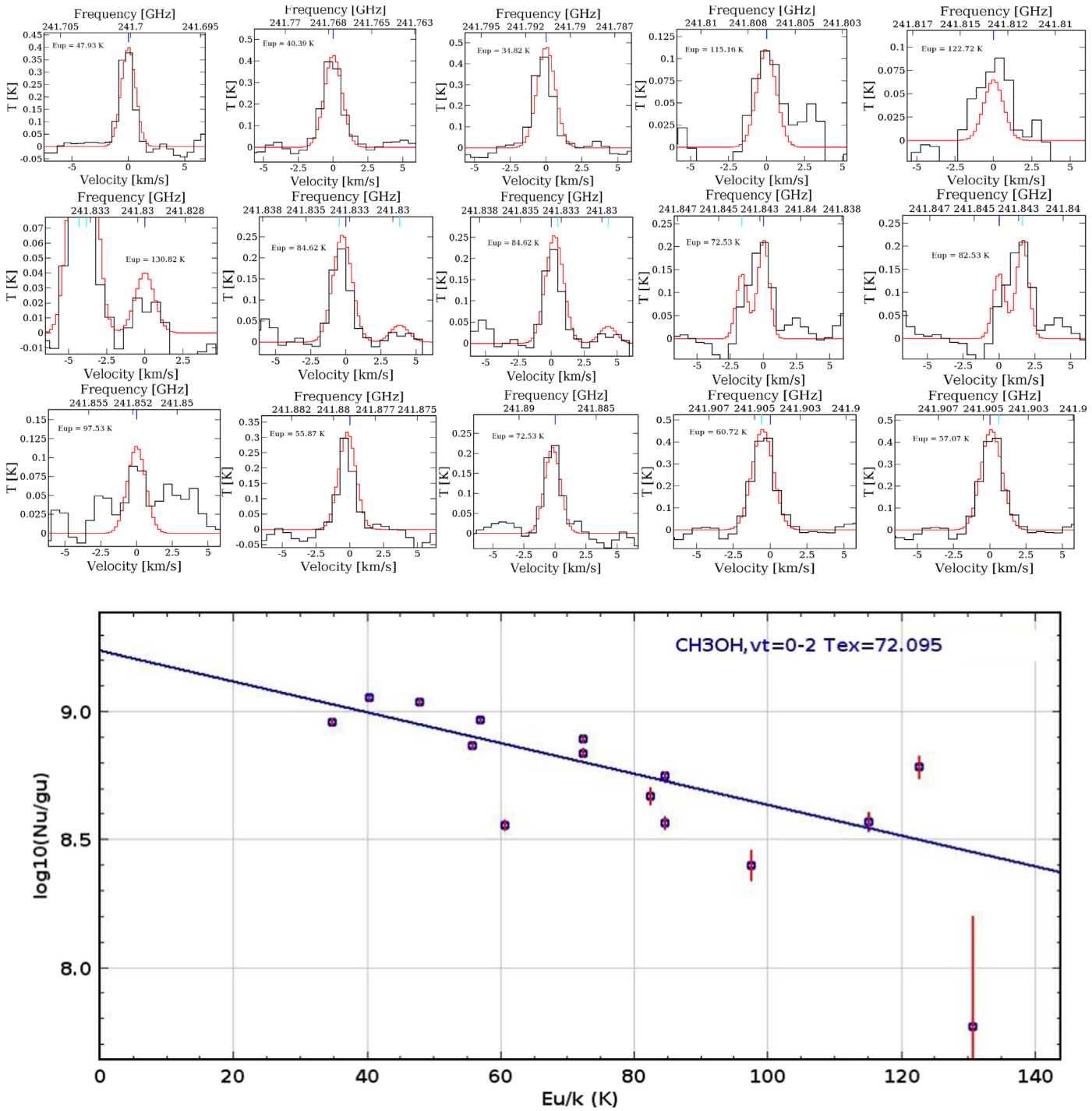

Figure 4. Rotational emission lines of CH_3OH toward comet ZTF (upper panel). In the spectra, the black lines are the observed spectra, and the red lines are the best-fit LTE model spectra of CH_3OH. The lower panel shows the rotational diagram of CH_3OH.

comet ZTF. After fitting the 2D Gaussian over the integrated intensity maps, we observed that the emitting regions of CH_3OH vary between 0.″47 and 0.″49. The derived emitting regions of CH_3OH are lower than the synthesized beam sizes of the integrated intensity maps, which shows that the integrated intensity maps are not resolved.

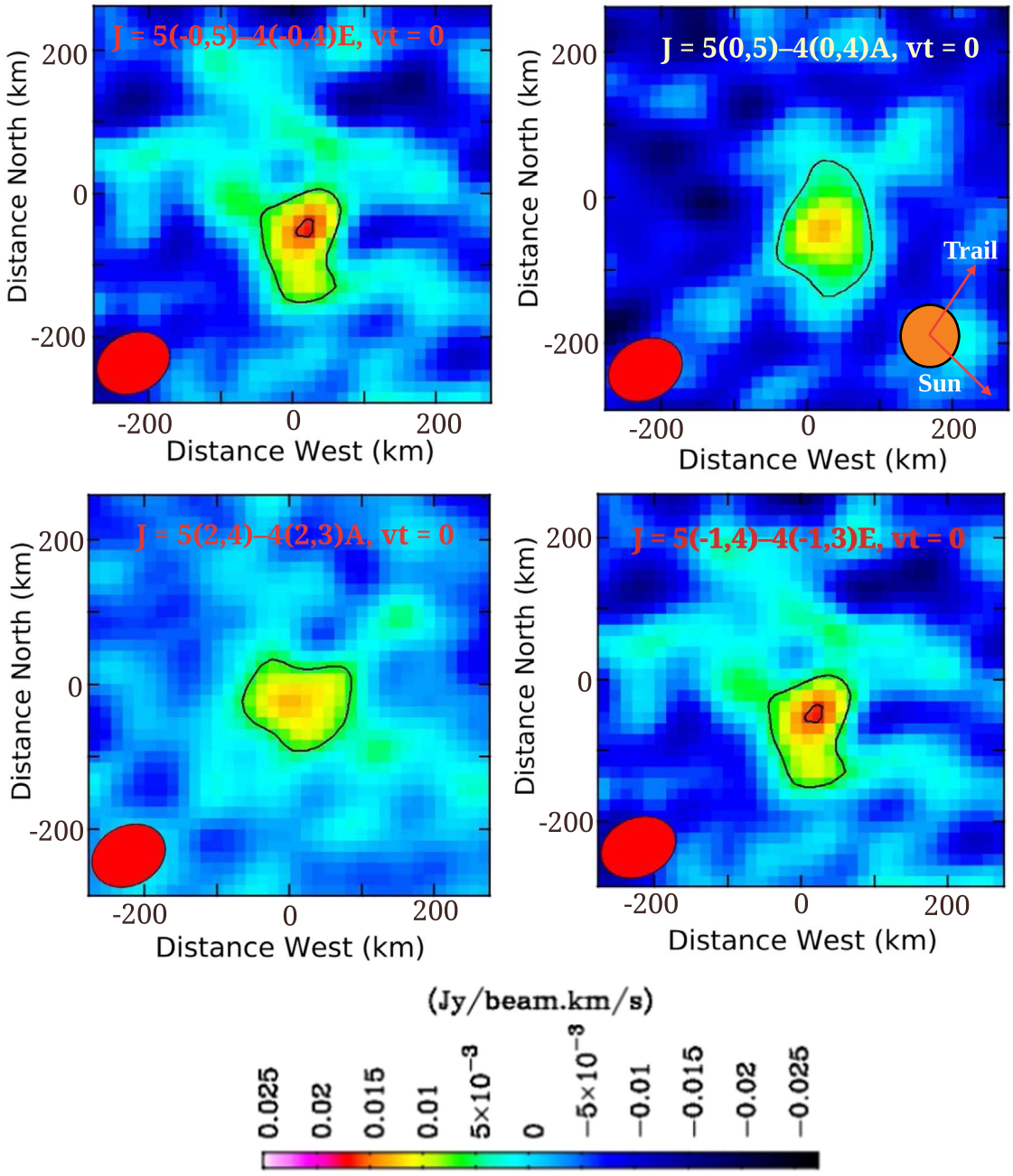

Figure 5. Integrated intensity maps of CH_3OH toward comet ZTF. The red-colored elliptical circles are the synthesized beam of the emission maps. The contour levels start at 3σ.

3.1.3. Production Rate of CH_3OH Toward Comet ZTF

To derive the production rate (Q) of CH_3OH using the line area ($\int T_{\rm mb} dV$) and rotational temperature toward comet ZTF, we relied on the following equation (Drahus et al. 2010)

$$Q = \frac{2}{\sqrt{\pi \ln 2}} \frac{k}{h} \frac{b\Delta v_{\rm exp}}{DI(T)\nu} \left(\exp\left(\frac{h\nu}{kT}\right) - 1 \right) \int T_{\rm mb} dV. \quad (2)$$

In the above equation, h and K are the Planck and Boltzmann constants respectively, b is a dimensionless factor whose value is 1.22, D is the diameter of the dish whose value is 12 m, Δ is the distance between Earth and comet, $I(T)$ indicates the integrated line intensity, which is defined in the CDMS line database, $v_{\rm exp}$ is the half-width at half maximum (HWHM) of the emission lines of CH_3OH, ν is the rest frequency of the

Table 4
Spectral Line Properties of CH_3OH Toward Comet ZTF

Frequency (GHz)	Quantum Number ($J'_{K'_a\Gamma'}$–$J''_{K''_a\Gamma''}$)	E_u (K)	A_{ij} (s^{-1})	g_{up}	$S\mu^2$ (Debye^2)	FWHM (km s^{-1})	$\int T_{mb}dV$ (K km s^{-1})	Optical Depth (τ)
241.700	5(−0,5)–4(−0,4)E, $v_t = 0$	47.93	6.04×10^{-5}	11	16.15	1.52 ± 0.23	0.62 ± 0.02	0.02
241.767	5(1,5)–4(1,4)E, $v_t = 0$	40.39	5.81×10^{-5}	11	15.53	1.54 ± 0.25	0.65 ± 0.01	0.03
241.791	5(0,5)–4(0,4)A, $v_t = 0$	34.82	6.05×10^{-5}	11	16.16	1.50 ± 0.32	0.67 ± 0.04	0.04
241.806	5(4,2)–4(4,1)A, $v_t = 0$	115.16	2.18×10^{-5}	11	5.82	1.57 ± 0.55	0.22 ± 0.06	0.02
241.813	5(4,2)–4(4,1)E, $v_t = 0$	122.72	2.18×10^{-5}	11	5.82	1.72 ± 0.62	0.17 ± 0.03	0.05
241.829	5(−4,1)–4(−4,0)E, $v_t = 0$	130.82	2.19×10^{-5}	11	5.85	1.62 ± 0.56	0.12 ± 0.02	0.03
241.832	5(3,3)–4(3,2)A, $v_t = 0$	84.62	3.87×10^{-5}	11	10.33	1.52 ± 0.26	0.31 ± 0.02	0.06
241.833	5(3,2)–4(3,1)A, $v_t = 0$	84.62	3.87×10^{-5}	11	10.33	1.52 ± 0.26	0.31 ± 0.02	0.06
241.842	5(2,4)–4(2,3)A, $v_t = 0$	72.53	5.12×10^{-5}	11	13.66	1.56 ± 0.52	0.37 ± 0.02	0.05
241.843	5(−3,3)–4(−3,2)E, $v_t = 0$	82.53	3.88×10^{-5}	11	10.36	1.56 ± 0.52	0.37 ± 0.02	0.05
241.852	5(3,2)–4(3,1)E, $v_t = 0$	97.53	3.89×10^{-5}	11	10.40	1.52 ± 0.24	0.13 ± 0.01	0.02
241.879	5(−1,4)–4(−1,3)E, $v_t = 0$	55.87	5.96×10^{-5}	11	15.92	1.53 ± 0.32	0.42 ± 0.06	0.03
241.887	5(2,3)–4(2,2)A, $v_t = 0$	72.53	5.12×10^{-5}	11	13.67	1.53 ± 0.38	0.35 ± 0.02	0.02
241.904	5(2,3)–4(2,2)E, $v_t = 0$	60.73	5.09×10^{-5}	11	13.59	1.58 ± 0.26	0.78 ± 0.02	0.03
241.904	5(−2,4)–4(−2,3)E, $v_t = 0$	57.07	5.03×10^{-5}	11	13.43	1.58 ± 0.27	0.78 ± 0.02	0.03

detected transition of CH_3OH, and $\int T_{mb}dV$ is the integrated line area of the molecule in km s^{-1}. For integrated line intensity values, we used $T = 75$ K because that temperature value is very close to the derived rotational temperature (72 ± 12 K) of CH_3OH. As per the CDMS molecular database, the value of I (75 K) is 1.45×10^{-4} nm^2 MHz. Equation (2) is well described in Drahus et al. (2010). Equation (2) is appropriate for estimating the production of CH_3OH toward comet ZTF because CH_3OH is found in LTE conditions and the radiated emission lines of CH_3OH are optically thin, which were emitted from the coma region. Using Equation (2), we estimate the production rates of CH_3OH based on all detected transitions, which are listed in Table 5. The error bars in production rate values were estimated based on the error values of v_{exp} and $\int T_{mb}dV$. After averaging those 15 production rate values, we obtain that the final production rate of CH_3OH toward comet ZTF is $(7.32 \pm 0.64) \times 10^{26}$ molecules s^{-1}. The production rate of CH_3OH toward comet ZTF estimated by Biver et al. (2024) using the Haser model is 8.78×10^{26} molecules s^{-1}, which is very close to our estimated production rate of CH_3OH using Equation (2). The abundance of CH_3OH with respect to H_2O toward comet ZTF is 1.52×10^{-2} (alternatively 1.52%), where the production rate of H_2O toward comet ZTF is 4.8×10^{28} molecules s^{-1} (Schleicher et al. 2023).

Table 5
Production Rate of CH_3OH Toward Comet ZTF

Frequency (GHz)	Quantum Number ($J'_{K'_a\Gamma'}$–$J''_{K''_a\Gamma''}$)	v_{exp} (km s^{-1})	Production Rate (Q) (molecule s^{-1})
241.700	5(−0,5)–4(−0,4)E, $v_t = 0$	0.76 ± 0.02	$(7.25 \pm 0.29) \times 10^{26}$
241.767	5(1,5)–4(1,4)E, $v_t = 0$	0.77 ± 0.03	$(6.82 \pm 0.62) \times 10^{26}$
241.791	5(0,5)–4(0,4)A, $v_t = 0$	0.75 ± 0.04	$(7.02 \pm 0.55) \times 10^{26}$
241.806	5(4,2)–4(4,1)A, $v_t = 0$	0.78 ± 0.02	$(7.36 \pm 0.78) \times 10^{26}$
241.813	5(4,2)–4(4,1)E, $v_t = 0$	0.86 ± 0.03	$(7.55 \pm 0.21) \times 10^{26}$
241.829	5(−4,1)–4(−4,0)E, $v_t = 0$	0.81 ± 0.06	$(7.82 \pm 0.30) \times 10^{26}$
241.832	5(3,3)–4(3,2)A, $v_t = 0$	0.76 ± 0.06	$(6.98 \pm 0.53) \times 10^{26}$
241.833	5(3,2)–4(3,1)A, $v_t = 0$	0.76 ± 0.05	$(6.97 \pm 0.55) \times 10^{26}$
241.842	5(2,4)–4(2,3)A, $v_t = 0$	0.78 ± 0.07	$(7.09 \pm 1.20) \times 10^{26}$
241.843	5(−3,3)–4(−3,2)E, $v_t = 0$	0.78 ± 0.06	$(7.10 \pm 1.22) \times 10^{26}$
241.852	5(3,2)–4(3,1)E, $v_t = 0$	0.76 ± 0.02	$(7.52 \pm 0.98) \times 10^{26}$
241.879	5(−1,4)–4(−1,3)E, $v_t = 0$	0.76 ± 0.02	$(7.36 \pm 0.76) \times 10^{26}$
241.887	5(2,3)–4(2,2)A, $v_t = 0$	0.76 ± 0.05	$(7.29 \pm 0.90) \times 10^{26}$
241.904	5(2,3)–4(2,2)E, $v_t = 0$	0.79 ± 0.06	$(7.82 \pm 0.55) \times 10^{26}$
241.904	5(−2,4)–4(−2,3)E, $v_t = 0$	0.79 ± 0.08	$(7.92 \pm 0.22) \times 10^{26}$
	Average production rate (Q_{CH_3OH})		$(7.32 \pm 0.64) \times 10^{26}$

3.1.4. Comparison of the Abundance of CH_3OH Between ZTF and Other Comets

Now, we compare the abundance of CH_3OH toward comet ZTF with other comets to understand the ice composition, as shown in Table 6. After comparison, we observe that the comet Austin (1990 V) exhibited a higher CH_3OH abundance. The abundance of CH_3OH toward comet ZTF is quite similar to that of comets P/Halley, C/2002 T7 (LINEAR), and C/2012 K1 (PanSTARRS). The abundance of CH_3OH toward ZTF is lower than that of P/Swift-Tuttle (1992), C/1996 B2 (Hyakutake), C/1995 O1 (Hale-Bopp), C/1999 H1 (Lee), 153P/2002 C1 (Ikeya-Zhang), C/2020 F3 (NEOWISE), 67P/

Table 6
Comparison of the Abundance of CH_3OH with Comet ZTF and Other Comets

Comet	Abundance of CH_3OH ($X = Q(CH_3OH)/Q(H_2O)$ in %)	Reference
C/2023 E3 (ZTF)	1.52	This study
Austin (1990 V)	5	Bockelée-Morvan et al. (1994a)
Levy (1990 XX)	0.91	Bockelée-Morvan et al. (1994a)
P/Swift-Tuttle (1992)	4	Bockelée-Morvan et al. (1994b)
P/Halley	1.71	Eberhardt et al. (1994)
C/1996 B2 (Hyakutake)	2.01	Biver et al. (1999b)
C/1995 O1(Hale-Bopp)	2.40	Bockelée-Morvan et al. (2000)
C/1999 H1 (Lee)	2.10	Mumma et al. (2001)
153P/2002 C1 (Ikeya-Zhang)	2.50	Disanti (2002)
C/2002 T7 (LINEAR)	1.50	Remijan et al. (2008)
C/2013 R1 (Lovejoy)	0.37	Agúndez et al. (2014)
C/2012 K1 (PanSTARRS)	1.33	Cordiner et al. (2017)
C/2012 F6 (Lemmon)	0.96	Bøgelund & Hogerheijde (2017)
C/2012 S1 (ISON)	0.48	Bøgelund & Hogerheijde (2017)
C/2020 F3 (NEOWISE)	2.30	Biver et al. (2022)
46P/Wirtanen	2.70	Cordiner et al. (2023)
67P/Churyumov-Gerasimenko	2.10	Biver et al. (2023)
C/2021 A1 (Leonard)	0.88	Biver et al. (2024)

Churyumov-Gerasimenko, and 46P/Wirtanen. Similarly, the abundance of CH_3OH toward ZTF is higher than that of Levy (1990 XX), C/2013 R1 (Lovejoy), C/2012 F6 (Lemmon), C/2012 S1 (ISON), and C/2021 A1 (Leonard). Since the abundance of CH_3OH toward ZTF is very similar to P/Halley, C/2002 T7 (LINEAR), and C/2012 K1 (PanSTARRS), there is a chance that the formation mechanism of CH_3OH and the icy compositions of these four comets may be the same.

3.1.5. Formation Mechanism of CH_3OH Toward Comet ZTF

High-resolution ALMA observations show that CH_3OH emits from the very deep cometary coma, which means there is a chance to form this molecule on the grain surface. Previous studies showed that if CH_3OH is formed in cometary ices, then this molecule may be an old part of the star formation regions because comets move from several star-forming regions in the ISM (Remijan et al. 2008). For the production of CH_3OH, two efficient reactions are available: (i) the radiative association of CH_3^+ and H_2O creates $CH_3OH_2^+$ ($CH_3^+ + H_2O \rightarrow CH_3OH_2^+$) and CH_3OH is formed when $CH_3OH_2^+$ recombines with an electron in the gas phase ($CH_3OH_2^+ + e^- \rightarrow CH_3OH$), and (ii) the subsequential hydrogenation of CO formed CH_3OH on the grain surface ($CO + 2H \rightarrow H_2CO + 2H \rightarrow CH_3OH$) (Remijan et al. 2008; Garrod 2019; Faggi et al. 2023).

Now, we compare our estimated abundance of CH_3OH with the modeled value of Garrod (2019) to understand the possible formation pathway of CH_3OH toward comet ZTF. The estimated abundance of CH_3OH toward a cometary atmosphere by Garrod (2019) is 1.3×10^{-2} (1.3%) at 5×10^9 yr (see Table 4 in Garrod 2019), which is very close to the observed abundance of CH_3OH toward comet ZTF. The modeled value of Garrod (2019) is also very close to the abundance of CH_3OH toward the other comets P/Halley, C/2002 T7 (LINEAR), and C/2012 K1 (PanSTARRS). That indicates CH_3OH may be formed via the subsequential hydrogenation of formaldehyde (H_2CO) on the grain surface of comets ZTF, P/Halley, C/2002 T7 (LINEAR), and C/2012 K1 (PanSTARRS). Similarly, the chemical models of Garrod (2019) show that CH_3OH is destroyed in the cometary atmosphere via photoionization processes ($CH_3OH + h\nu \longrightarrow CH_2 + H_2O$).

3.2. Results Based on GMRT Data

After analyzing the GMRT data, we did not detect the dust continuum emission from the comet ZTF. The upper limit flux density of comet ZTF at frequency 1250 MHz was $\leqslant 1.50 \pm 0.21$ mJy, where the synthesized beam size of the continuum emission image was $2\farcs66 \times 1\farcs50$. After that, we extracted the atomic spectra by making a $5\farcs0$ diameter circular region over the spectral images. After analyzing the atomic spectra, we could not detect the H I line at 1420 MHz. We estimate the upper limit column density of atomic H I using the following equation (Chengalur et al. 2013)

$$N_{\rm HI} = 1.823 \times 10^{18} \int T_s \tau dV. \quad (3)$$

In the above equation, T_s indicates the spin temperature of H I in K, τ is the optical depth of the H I spectra, and $\int dv$ is the integrated area in km s^{-1}. Equation (3) is well described in Pal & Manna (2024). We used the value of $T_s = 100$ K (Paris 2017),

$\tau \leqslant 0.23$, and $\int dv \leqslant 0.36$. Applying Equation (3), we found the upper limit column density of atomic H I is $\leqslant 1.50 \times 10^{19}\,\mathrm{cm}^{-2}$.

4. Conclusion

In this article, we present the radio and millimeter-wavelength studies of comet ZTF using the GMRT band L and the ALMA band 6. The principal conclusions derived from this study are summarized below:

1. We detected the dust continuum emission from comet ZTF using ALMA between the frequency range of 223.85 and 243.55 GHz. The activity of dust production ($Af\rho$) of comet ZTF is 2280 ± 50 cm.
2. We detected the rotational emission lines of CH_3OH toward comet ZTF using ALMA. A total of 15 transition lines of CH_3OH is detected. Using the LTE model, we found the column density and excitation temperature of CH_3OH are $(4.50 \pm 0.25) \times 10^{14}\,\mathrm{cm}^{-2}$ and 70 ± 3 K respectively. From the integrated emission maps, we observed that the emission lines of CH_3OH emit from the coma region of the comet ZTF. The production rate of CH_3OH on 2023 March 2 is $(7.32 \pm 0.64) \times 10^{26}$ molecules s^{-1}. The abundance of CH_3OH with respect to H_2O in the coma of the comet is 1.52%. We compared our derived abundance of CH_3OH with the modeled value of Garrod (2019), and we noticed that the observed and modeled values are quite similar. We claim that CH_3OH is formed via the subsequential hydrogenation of formaldehyde (H_2CO) on the grain surface of comet ZTF.
3. From the GMRT data, continuum emission and an emission line of atomic H I are not detected. The upper limit for flux density of comet ZTF at frequency 1250 MHz is $\leqslant 1.50 \pm 0.21$ mJy. The upper limit for column density of atomic H I toward the comet ZTF is $\leqslant 1.50 \times 10^{19}\,\mathrm{cm}^{-2}$.

Acknowledgments

We thank the anonymous reviewers for their helpful comments, which helped to make the manuscript stronger. A. M. acknowledges the Swami Vivekananda Merit Cum Means Scholarship (SVMCM), Government of West Bengal, for financial support for this research. Supplementary materials, including additional plots and data, are available from the corresponding author upon reasonable request. We are grateful to the staff of the Giant Metrewave Radio Telescope (GMRT) for their support during the observation. The raw data of comet ZTF presented in this paper can be accessed through the GMRT archive using the proposal code ddtC267. The GMRT is operated by the National Centre for Radio Astrophysics (NCRA), a facility of the Tata Institute of Fundamental Research (TIFR). This paper makes use of the following ALMA data: ADS /JAO.ALMA#2022.1.00997.T. ALMA is a partnership of ESO (representing its member states), NSF (USA), and NINS (Japan), together with NRC (Canada), MOST and ASIAA (Taiwan, China), and KASI (Republic of Korea), in co-operation with the Republic of Chile. The joint ALMA Observatory is operated by ESO, AUI/NRAO, and NAOJ. We also acknowledge Gideon van Buitenen (http://astro.vanbuitenen.nl/comet/2022E3) for providing the track of comets and images of the inner solar system.

Conflicts of Interest

The authors declare no conflict of interest.

References

Agúndez, M., Biver, N., Santos-Sanz, P., Bockelée-Morvan, D., & Moreno, R. 2014, A&A, 564, L2
A'Hearn, M. F., Schleicher, D. G., Millis, R. L., Feldman, P. D., & Thompson, D. T. 1984, AJ, 89, 579
Altwegg, K., Balsiger, H., Bar-Nun, A., et al. 2016, SciA, 2, e1600285
Altwegg, K., & Bockelée-Morvan, D. 2003, SSRv, 106, 139
Ball, J. A., Gottlieb, C. A., Lilley, A. E., & Radford, H. E. 1970, ApJL, 162, L203
Biver, N., & Bockelée-Morvan, D. 2019, ESC, 3, 1550
Biver, N., Bockelée-Morvan, D., Colom, P., et al. 1999a, EM&P, 78, 5
Biver, N., Bockelée-Morvan, D., Crovisier, J., et al. 1999b, AJ, 118, 1850
Biver, N., Bockelée-Morvan, D., Crovisier, J., et al. 2000, AJ, 120, 1554
Biver, N., Bockelée-Morvan, D., Crovisier, J., et al. 2023, A&A, 672, A170
Biver, N., Bockelée-Morvan, D., Handzlik, B., et al. 2024, A&A, 690, A271
Biver, N., Boissier, J., Bockelée-Morvan, D., et al. 2022, A&A, 668, A171
Bockelée-Morvan, D., Calmonte, U., Charnley, S., et al. 2015, SSRv, 197, 47
Bockelée-Morvan, D., Crovisier, J., Colom, P., & Despois, D. 1994a, A&A, 287, 647
Bockelée-Morvan, D., Lis, D. C., Wink, J. E., et al. 2000, A&A, 353, 1101
Bockelée-Morvan, D., Padman, R., Davies, J. K., & Crovisier, J. 1994b, P&SS, 42, 655
Bolin, B., Masci, F., Duev, D., et al. 2024, MNRAS, 527, L42
Bolin, B. T., Masci, F. J., Ip, W.-H., et al. 2022, MPEC, 2022, F13
Booth, A. S., Walsh, C., Terwisscha van Scheltinga, J., et al. 2021, NatAs, 5, 684
Bøgelund, E. G., & Hogerheijde, M. R. 2017, A&A, 604, A131
CASA Team, Bean, B., Bhatnagar, S., et al. 2022, PASP, 134, 114501
Chen, L. F., Li, D., & Quan, D. 2022, ApJ, 928, 175
Cordiner, M. A., Biver, N., Crovisier, J., et al. 2017, ApJ, 837, 177
Cordiner, M. A., Roth, N. X., Milam, S. N., et al. 2023, ApJ, 953, 59
Chengalur, J. N., Kanekar, N., & Roy, N. 2013, MNRAS, 432, 3074
Drabek-Maunder, E., Greaves, J., Fraser, H. J., Clements, D. L., & Alconcel, L.-N. 2019, IJAsB, 18, 25
Drahus, M., Kuppers, M., Jarchow, C., et al. 2010, A&A, 510, A55
Disanti, M. A., dello Russo, N., Magee-Sauer, K., et al. 2002, ESASP, 500, 571
Eberhardt, P., Meier, R., Krankowsky, D., & Hodges, R. R. 1994, A&A, 288, 315
Ehrenfreund, P., & Charnley, S. B. 2000, ARA&A, 38, 427
Faggi, S., Lippi, M., Mumma, M. J., & Villanueva, G. L. 2023, PSJ, 4, 8
Garrod, R. T. 2019, ApJ, 884, 69
Gillan, A. F., Fitzsimmons, A., Denneau, L., et al. 2024, PSJ, 5, 25
Greenberg, J. M. 1982, Comets. (A83-13376 03-90) (Tucson, AZ: Univ. Arizona Press), 131
Hadraoui, K., Cottin, H., Ivanovski, S. L., et al. 2019, A&A, 630, A32
Hartogh, P., Lis, D. C., Bockelée-Morvan, D., et al. 2011, Natur, 478, 218
Herbst, E., & van Dishoeck, E. F. 2009, ARA&A, 47, 427
Jayakrishnan, R., Dev L, R., & Aalim, M. 2023, RNAAS, 7, 44
Jehin, E., Donckt, M. V., Manfroid, J., & Moulane, Y. 2022, ATel, 15743, 1

Jehin, E., Donckt, M. V., Manfroid, J., et al. 2023, ATel, 15973, 1
Kurucz, R. L., Furenlid, I., Brault, J., & Testerman, L. 1984, Solar Flux Atlas from 296 to 1300 nm (Sunspot, NM: National Solar Observatory)
Liu, B., & Liu, X. 2024, A&A, 683, A51
Lellouch, E., Moreno, R., Bockelée-Morvan, D., Biver, N., & Santos-Sanz, P. 2022, A&A, 659, L1
Manigand, S., Jørgensen, J. K., Calcutt, H., et al. 2020, A&A, 635, A48
Manna, A., & Pal, S. 2024, NewA, 109, 102199
Müller, H. S. P., Schlöder, F., Stutzki, J., & Winnewisser, G. 2005, JMoSt, 742, 215
Mumma, M. J., McLean, I. S., DiSanti, M. A., et al. 2001, ApJ, 546, 1183
Pal, S., & Manna, A. 2024, JApA, 45, 10
Paris, A. 2017, arXiv:1706.03259
Perley, R. A., & Butler, B. J. 2017, ApJS, 230, 7
Rau, U., & Cornwell, T. J. 2011, A&A, 532, A71
Remijan, A. J., Milam, S. N., Womack, M., et al. 2008, ApJ, 689, 613
Schleicher, D. G. 2006, Icar, 181, 442
Schleicher, D. G., Knight, M. M., & Skiff, B. A. 2023, in Asteroids, Comets, Meteors Conf. (Houston, TX: LPI Contribution), 2851
Schleicher, D. G., Millis, R. L., & Birch, P. V. 1998, Icar, 132, 397
Thiel, V., Belloche, A., Menten, K. M., Garrod, R. T., & Müller, H. S. P. 2017, A&A, 605, L6
Vastel, C., Bottinelli, S., Caux, E., Glorian, J.-M., & Boiziot, M. 2015, in SF2A-2015: Proc. Annual Meeting of the French Society of Astronomy and Astrophysics, ed. F. Martins et al. (Paris: French Society of Astronomy & Astrophysics), 313
Womack, M., Stern, S. A., & Festou, M. C. 1997, P&SS, 45, 711